IEEE Access
Multidisciplinary | Rapid Review | Open Access Journal

Received 10 April 2024, accepted 9 May 2024, date of publication 17 May 2024, date of current version 24 May 2024.

Digital Object Identifier 10.1109/ACCESS.2024.3402224

RESEARCH ARTICLE

A Hybrid Fault Detection Method for Hairpin Windings Integrating Physics Model and Machine Learning

YU ZHANG[1], YIXIN HUANGFU[1], (Member, IEEE), YOUSSEF ZIADA[2], AND SAEID HABIBI[1], (Member, IEEE)

[1]Department of Mechanical Engineering, McMaster University, Hamilton, ON L8S 4L8, Canada
[2]Battery Manufacturing Engineering, Ford Motor Company, Dearborn, MI 48120, USA

Corresponding author: Yu Zhang (zhang21@mcmaster.ca)

This work was supported in part by Canada Research Chairs Program.

ABSTRACT This study proposes a hybrid fault detection methodology for detecting epoxy faults in hairpin-based stator windings of electric motors. The hybrid methodology integrates a model-based approach for feature extraction and a data-driven approach for fault classification. A new lumped-parameter equivalent circuit model specifically for hairpin windings is developed. It can accurately simulate the high-frequency impedance behaviors of hairpin windings and physically interpret the distinction of the measurement curves under different epoxy configurations. Using system identification, the parameters of this new model are identified to extract the features of phase windings, reflecting different fault conditions by varying the parameters in distinct ranges. Fault classification is implemented using a data-driven method to distinguish the underlying patterns, which is difficult to achieve by conventional threshold limit checking due to the inevitably introduced noise and uncertainties. Principal Component Analysis (PCA) is applied to refine the features, followed by a Support Vector Machine (SVM) performing fault classification. The proposed hybrid methodology successfully detects epoxy-related fault conditions, providing a new strategy for fault detection.

INDEX TERMS Stator windings, model-based, data-driven, fault detection, hybrid strategy.

I. INTRODUCTION

Brushless DC motors (BLDCs) have become the dominant mode of propulsion in the automotive industry because of their high power density and control simplicity [1]. With state-of-the-art techniques, hairpin windings take the place of conventional wound wire windings in stators to generate magnetic fields, drive the rotor and output mechanical energy. Detecting incipient faults of hairpin windings in manufacturing lines is an important consideration for production quality assurance.

Researchers have primarily based existing studies of stator winding models [2], [3], [4], [5] on conventional wound wire windings. However, simulations using such models for characterizing hairpin windings can produce significant errors because they do not account for variations of the hairpin winding's inductance and resistance under different high-frequency excitations. Therefore, this study has developed a specific model to reproduce the high-frequency characteristics of hairpin windings.

Based on conventional stator winding models, the new model introduces one additional inductance parameter to account for the skin and proximity effects as well as parameter changes due to different excitation frequencies. The developed model can accurately simulate the high-frequency impedance behaviors of hairpin windings in the frequency domain and physically interpret the distinction of measurement curves under different physical configurations.

This study also applies the new model for Fault Detection and Diagnosis (FDD) by combining machine learning methodologies. A hybrid FDD model is proposed, integrating a model-based approach for feature extraction and a data-driven approach for fault classification. First, parameters are extracted from a physical model to reflect different

The associate editor coordinating the review of this manuscript and approving it for publication was Yue Zhang.

configurations of hairpin windings with varying distinct ranges. Then, a trained machine learning model effectively removes noise, distinguishes underlying patterns, and provides fault detection or classification results. The hybrid methodology leverages the strengths of both approaches and overcomes their deficiencies, achieving high FDD accuracy while retaining interpretability.

This paper is organized as follows. Section II reviews related studies on model-based and data-driven fault detection methods. Section III outlines the proposed hybrid methodology and its components. Section IV introduces the acquired measurement data used as the input for fault detection. Section V develops a lumped-parameter equivalent circuit model and identifies the parameters using system identification. Section VI performs fault classification using a data-driven method. Section VII presents the conclusions of this study.

II. RELATED STUDIES

Model-based and data-driven approaches are two common methods in FDD. Model-based approaches can diagnose and isolate faults straightforwardly with a physical understanding of the system. On the other hand, data-driven approaches exhibit remarkable adaptability for various systems, as they do not necessarily require prior knowledge of the system. The details of each approach are as follows.

A. MODEL-BASED APPROACHES

In model-based approaches, the physical relationships of the objective system are established in the form of a mathematical representation [6], [7]. The inconsistencies between the measurements and their predicted values from the models are calculated and compared, referred to as residuals. The residuals are then checked against the threshold limits and are used as indicators for detecting faults.

Physics-based stator winding modeling can be presented in either the frequency domain [2], [8], [9] or time domain [10], [11], [12]. Time-domain analysis focuses on signal variation over time whereas frequency domain is a spectral characterization of the system.

Most available models of stator windings are developed based on conventional wound wire windings. Although some behaviors of wound wire windings are similar to those of hairpin windings, such models cannot adequately capture all the characteristics of hairpin windings within BLDCs. Detecting faults in hairpin windings based on these models is not feasible. Therefore, a specific model for hairpin windings must be developed before implementing model-based approaches.

B. DATA-DRIVEN APPROACHES

Data-driven approaches extract underlying information from historical data or measurements and achieve fault detection by conducting classifications [13], [14]. With emerging artificial intelligence (AI) techniques and data availability, underlying patterns in data are substantially extracted using data-driven approaches, which include both supervised and unsupervised approaches. Supervised approaches perform training based on labeled samples. On the other hand, unsupervised approaches have no prior information about the training samples; this is also referred to as clustering techniques.

Since labels are available in this study, e.g., the health status of stator windings, supervised learning algorithms are of research interest. One popular machine-learning algorithm is the Support Vector Machine (SVM) [15]. It is suitable for nonlinear multilabel classification tasks and achieves good performance for small samples. References [15] and [16] applied SVM to diagnose different classes of faults (turn faults and ground faults) within stator windings after different techniques were used to extract features, e.g., spectral analysis and Stockwell transform.

Artificial Neural Networks (ANNs) perform successfully in pattern recognition and nonlinear function approximation tasks [6], [17]. The capabilities for adaptive learning and handling noisy or incomplete data make ANNs a powerful machine-learning tool in FDD. Reference [18] collected both voltage and current data to diagnose shorted-turn, phase-to-ground and coil-to-coil faults within electric motors by using a developed ANN. Reference [19] employed ANNs on stator current signal data to detect insulation failure. This study showed that additional feature extraction could improve the detection accuracy.

Deep learning, which is a subset of machine learning, has become popular nowadays due to its deep architecture capturing high-level features. Unlike traditional machine learning demanding a separate feature extraction process, deep learning combines feature extraction and classification into one step and can work directly on the raw data [20], [21]. Some commonly employed deep learning algorithms are reviewed.

Convolutional Neural Networks (CNNs) are well suitable for processing 2-D data [22], like images. Local receptive fields, weight sharing, and spatial sub-sampling are the three main architectural foundations of CNN structure [14]. Both [23] and [24] tried to detect interturn short circuits based on current signal data. Reference [23] employed CNNs directly on the raw signal data, conducting both feature extraction and classification within the same process whereas [24] firstly used bispectrum analysis to generate 2-D data, followed by a CNN performing classification.

Recurrent Neural Networks (RNNs) [25], [26] are specialized for processing sequential data with variable length. They introduce a hidden state used as internal memory, which contains information on all the previous elements in the sequential data. To avoid vanishing or exploding gradient problems within RNNs, Long Short-Term Memory networks (LSTMs) are developed, creating shortcut paths across time steps to maintain long-term dependencies. Reference [27] applied LSTMs directly on time-domain current data to detect a three-phase short circuit to ground fault and achieved superior detection accuracy compared to

conventional Motor Current Signature Analysis (MCSA), Multi-Layer Perceptron (MLP) and 1D-CNN in this specific case. Reference [28] measured vibration signals to diagnose the severity of open circuit faults within stator windings. Both raw data and extracted features were used to train the LSTM separately and using extracted features as the input presented higher detection accuracy.

C. LIMITATIONS

Both model-based and data-driven approaches have their limitations. Model-based approaches always require expert knowledge to construct a model as a baseline to compare other measurements. It is not always feasible to develop such an accurate model for complex systems while accounting for noise and uncertainties. The performance of data-driven approaches significantly depends on the quality and quantity of the available data. Such requirements for data are difficult to satisfy due to the practical and environmental restrictions, e.g., in manufacturing lines.

From the above analysis, model-based and data-driven approaches complement each other. Hybrid fault detection methods [29], [30] that integrate both approaches enhance the detection effectiveness and increase the detection accuracy. In this study, a hybrid fault detection methodology based on a novel high-frequency modeling of hairpin windings and a machine-learning classification method is proposed.

III. THE HYBRID FAULT DETECTION METHODOLOGY

The proposed hybrid fault detection method is illustrated in Fig. 1. This method primarily relies on a model-based block (represented by a dashed blue block) to extract the features of hairpin windings and a data-driven block (represented by a dashed orange block) to perform fault classification. These two blocks are connected in series where the output of the first block is the input of the second block.

High-frequency impedance data of hairpin windings are measured and used as the primary input for the whole fault detection method. Based on conventional equivalent-circuit models of wound wire windings, a physics-based high-frequency model is developed specifically for hairpin windings to account for the skin and proximity effects. By minimizing errors between measured impedance data and corresponding predicted values of the physics-based model under the same excitation frequencies, parameters within the physical model are identified using system identification and are used as extracted features to input into the subsequent data-driven block to conduct fault classification.

Within the data-driven fault classification block, extracted features are first manipulated to be compatible with the downstream classification process. Then a data visualization is performed to get insight into the structure of the feature data and guide the detection algorithm selection. Before applying Principal Component Analysis (PCA) to further refine data, feature data are split into both training and testing sets. A portion of data samples are first processed with downstream classification procedures for training, determining the optimal parameters and weights of the learning method. The rest are then used as testing data to predict the corresponding class labels. The proposed machine learning model based on an SVM successfully classifies both healthy and faulty stator windings and fault detection results are output.

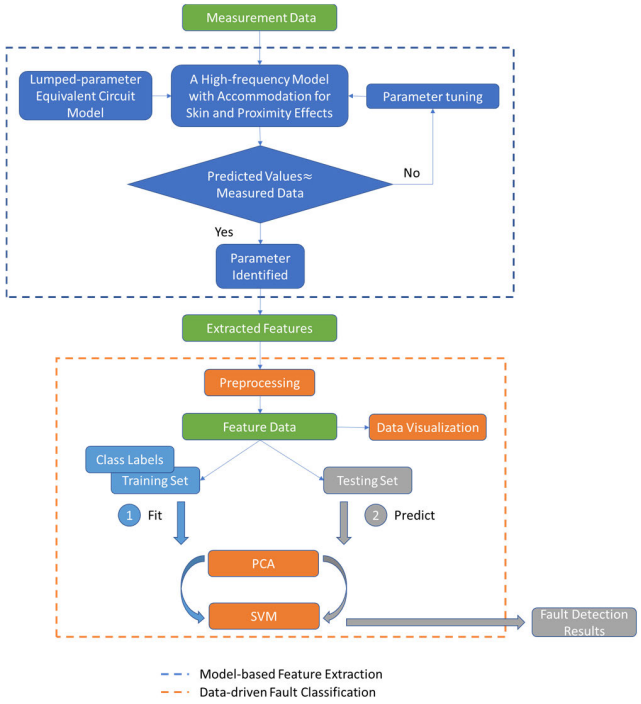

FIGURE 1. The hybrid fault detection methodology.

The measurement data is elaborated in the next section and the implementation of each block is detailed in Sections V and VI respectively.

IV. MEASUREMENT DATA

The experimental setup is the same as the system used in our previous work [31]. The details of the available stator samples, specific health status and fault types, the experimental setup and the format of acquired data are detailed in Appendix.

Fig. 2 shows the acquired measurement data of the phase 2 winding for all ten stator samples; similar trends are observed in other phase windings of the stators. The plot presents magnitude and phase angles across frequencies ranging from 20 kHz to 1 MHz, with the magnitude and frequency plotted on a logarithmic scale to clearly show distinctions between the plotted curves. Healthy stators 1 to 5 are shown by solid lines whereas faulty stators 6 to 10 are represented as dashed lines.

In Fig. 2, each phase winding measurement reveals the presence of a pair of parallel resonance frequencies with significant dissipative phenomena. Stators 9 and 10 (presented in red and black dashed lines, respectively), which lack epoxy coating, exhibit higher resonance frequencies and larger impedance magnitudes compared to other stators with

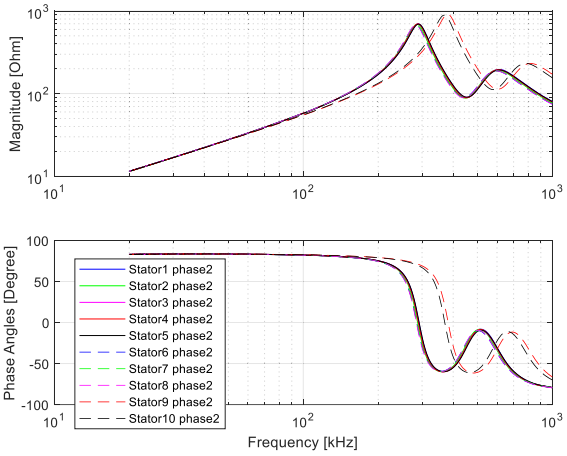

FIGURE 2. Impedance measurement data within ten stators.

epoxy coating. Furthermore, stators 6 to 8, with epoxy faults, exhibit a resonance frequency shift in contrast to the healthy stators (stators 1 to 5). This can be observed in Fig. 7 within Subsection V-E, where resonance frequencies f_1 and f_2 show distinct varying ranges between healthy and faulty stators. The measurements show that the resonance frequencies and dissipative phenomenon of hairpin windings are significantly affected by different epoxy configurations, a factor of critical importance in high-frequency impedance behaviors. These two factors can be promising indicators of epoxy-related fault conditions.

Though some distinctions are observed in Fig. 2, it is still not feasible to perform an effective diagnosis based on the raw measured data. To effectively distinguish stator windings with faulty conditions, these measured data are input to the model-based block in Fig. 1 to extract significant features, where a physics-based high-frequency model of phase windings is developed and utilized; details are presented in the next section.

V. MODEL-BASED FEATURE EXTRACTION

This section extracts features of measurement data using a model-based approach. Initially, a conventional model based on wound wire windings is introduced, followed by its limitations to characterize the hairpin windings. To account for the skin and proximity effects of hairpin windings, a novel high-frequency model is established specifically for hairpin windings. The parameters of the developed equivalent circuit model are identified using system identification.

A. A CONVENTIONAL MODEL

As discussed in Section II-A, an accurate model is essential in model-based approaches. Most available high-frequency models are based on wound wire windings [2], [10]. These models represent the characteristics of stator windings using a lumped-parameter equivalent circuit and a typical example is illustrated in Fig. 3, adapted from [2].

The parameters of this model represent a clear physical significance, as described in TABLE 1.

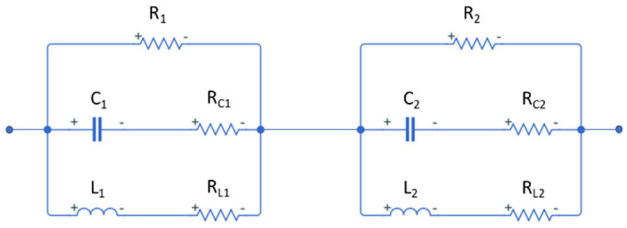

FIGURE 3. A conventional lumped-parameter equivalent circuit model.

TABLE 1. Physical significance of parameters.

Parameters	Physical Significance
R_1, R_2	Resistance accounts for the dissipative effect caused by iron losses
C_1, C_2	Capacitance of stator windings, including parasitic capacitance
L_1, L_2	Inductance of stator windings, representing both internal inductance and leakage inductance
R_{C1}, R_{C2}	Resistance represents dissipative phenomena due to high-frequency capacitive currents
R_{L1}, R_{L2}	Winding resistance

B. LIMITATIONS

Since the conventional model is established based on wound wire windings, the characteristics of hairpin windings are not adequately represented. Therefore, simulations of hairpin windings based on such models are prone to errors. Fig. 4 presents a comparison between the simulation results based on the conventional model (red curves) and the actual measurement data (blue curves). The procedures and implementation of this simulation are detailed in Subsections V-D and V-E.

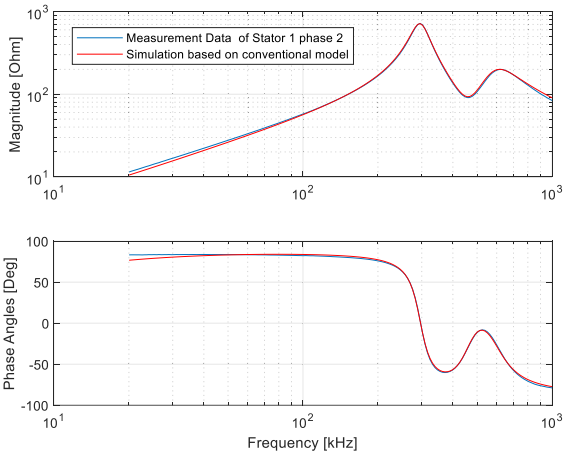

FIGURE 4. Simulation of hairpin windings based on the conventional model.

Fig. 4 uses phase winding 2 of stator 1 as an example of healthy. Evidently, the simulation demonstrates a favorable agreement with the measurement data above 100 kHz. This can be attributed to the model's inclusion of two resonance frequencies, ω_1 and ω_2, which effectively characterize the

two peak magnitudes in the impedance variations. The resonance frequencies ω_1 and ω_2 are approximated by reactance parameters L_1, L_2, C_1 and C_2 [32], [33]. Since the resistances $R_{L1}, R_{L2}, R_{C1}, R_{C2}$ are much smaller than the reactance parameters, such resistances are often neglected [10], and the equations to obtain $\omega_1$and ω_2 are:

$$\omega_1^2 = (2\pi f_1)^2 = \frac{1}{L_1 C_1} \tag{1}$$

$$\omega_2^2 = (2\pi f_2)^2 = \frac{1}{L_2 C_2} \tag{2}$$

where ω_1 and ω_2 are the resonance angular frequencies and f_1 and f_2 are the resonance frequencies in Hz.

However, a significant discrepancy between the measurement data and simulation is observed under frequencies of 100 kHz. These discrepancies in the simulation can be primarily attributed to variations of L, the inductance of a phase winding and R_L, the resistance of the inductor. These two values vary with respect to excitation frequencies, due to electromagnetic interactions between the varying magnetic fields and high-frequency currents flowing into the windings [34].

1) INDUCTANCE L VARIATION

For hairpin-based winding modeling, the inductance of phase windings should be presented as [2] and [35]

$$L = L_{con} + L_{var} \tag{3}$$

where L_{con} is a constant component, while L_{var} is a variation in inductance L.

L_{con} represents the inductance when part of phase windings extends beyond the iron core and is exposed to surrounding air, as shown in Fig 11. (a) and (b) within Appendix. This component remains constant and does not change with excitation frequency. On the other hand, L_{var} simulates the additional inductance that arises when the majority of the phase windings are installed in an iron core; this component varies with respect to the excitation frequency.

The component L_{var} is affected by eddy currents generated within iron core laminations due to electromagnetic effects. At high frequencies, more eddy currents are generated which produces shielding effects that hinder magnetic flux line penetration through iron core laminations. Consequently, this results in a reduction of L_{var} values. At low frequencies, less eddy currents are produced where magnetic lines penetrate the iron core, thereby increasing L_{var} values.

L_{var} can be estimated as a power function of the excitation frequency f.

$$L_{var} = a_1 \times (f)^{a_2} \tag{4}$$

where a_1 and a_2 are variables; f is the excitation frequency.

2) RESISTANCE R_L VARIATION

Due to the skin and proximity effects [34], [36], resistance R_L varies in response to changes in excitation frequencies. Similar to inductance L, resistance R_L is composed of two components.

$$R_L = R_{L-con} + R_{L-var} \tag{5}$$

where R_{L-con} is a constant component and R_{L-var} is a variable component.

R_{L-var} shows different behaviors at low and high frequencies and can be presented as a quadratic response at low frequencies, while demonstrating a square root response at high frequencies [9], [35].

$$R_{L-var-low} = a_3 \times (f)^2 + a_4 \times f + a_5 \tag{6}$$

$$R_{L-var-high} = a_6 \times \sqrt{f + a_7} \tag{7}$$

where a_3 - a_7 are variables; $R_{L-var-low}$ and $R_{L-var-high}$ present behavior of component R_{L-var} at low and high frequencies separately.

3) LIMITATIONS OF INVOLVING L AND R_L VARIATION

In order to characterize the hairpin windings, the conventional model must incorporate the variables discussed above. Owing to the curse of dimensionality [37], which depicts that general problems become more difficult to solve with increased dimensionality, introducing 7 additional variables (a_1 - a_7) within the parameter vector significantly increases the complexity of the model. Since the subsequent parameter identification applies iterative numerical techniques, involving more variables makes optimization challenging in finding the optimal set of variables, where a total of 17 variables needs to be accommodated. Additionally, the space of the search domain during the optimization expands exponentially with dimensionality, leading to increased computational cost. Therefore, a novel high-frequency model particularly for hairpin windings is developed in the next subsection.

C. A NOVEL HIGH-FREQUENCY MODEL

Based on the discussion above, it becomes evident that R_{L1} plays a crucial role in characterizing the frequency response of the hairpin windings, particularly when the excitation frequency is below 100 kHz. The variation in resistance R_{L1} with excitation frequencies is due to the skin and proximity effects caused by electromagnetic induction [38], [39]. This phenomenon is reasonably accounted for by adding an inductance L_P parallelly to R_{L1} in the new model, see Fig. 5.

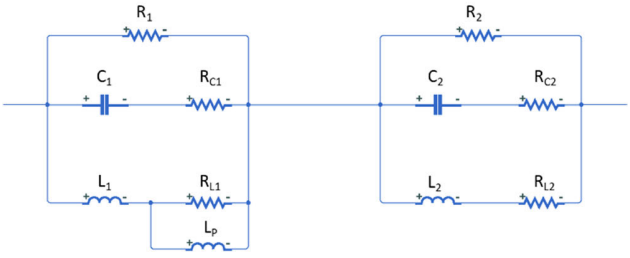

FIGURE 5. A novel equivalent-circuit model to accommodate high-frequency dynamics of hairpin windings.

The impedance behavior of the new model is:

$$\hat{Z} = \frac{1}{\frac{1}{R_1} + \frac{1}{2\pi f L_1 i + \frac{1}{\frac{1}{R_{L1}} + \frac{1}{2\pi f L_P i}}} + \frac{1}{\frac{1}{2\pi f C_1 i} + R_{C1}}} + \frac{1}{\frac{1}{R_2} + \frac{1}{2\pi f L_2 i + R_{L2}} + \frac{1}{\frac{1}{2\pi f C_2 i} + R_{C2}}} \tag{8}$$

where $\hat{Z}$ is the complex impedance; i presents the imaginary part and L_P represents skin and proximity effects caused by electromagnetic induction.

The newly proposed model avoids the necessity of introducing numerous variables to accommodate for inductance and resistance variations. Keeping the elements constant within the circuit, the model can accurately characterize the high-frequency response of phase windings. In comparison to the conventional models, this new model reduces the variable quantities, the complexity of the model and the computational cost. Meanwhile, the simulation accuracy significantly increases, as detailed in Subsection. E.

D. PARAMETER IDENTIFICATION

Parameters of the equivalent circuit model are identified using system identification [37], [40]. The specific procedures are illustrated in Fig. 6.

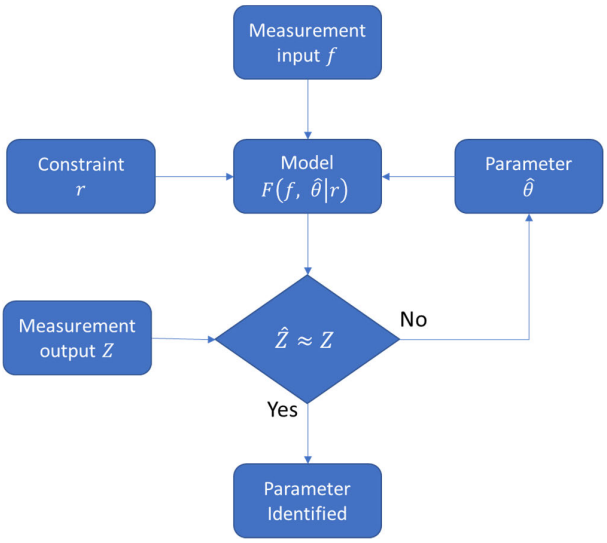

FIGURE 6. Parameter identification using system identification.

Measurement data are already collected in Section IV, including both input and output data, which are necessary for model validation. With measured excitation frequencies f as input, the high-frequency lumped-parameter model predicts impedance $\hat{Z}$ based on initial parameters $\hat{\theta}$ under constraints r, i.e., resonance frequencies.

The phase winding model in (8) is represented as

$$\hat{Z} = F\left(f, \hat{\theta} \,|\, r\right) \tag{9}$$

$$\hat{\theta} = [R_1, R_{C1}, R_{L1}, R_2, R_{C2}, R_{L2}, L_1, L_2, L_P]^T \tag{10}$$

$$r = [\omega_1, \omega_2]^T \tag{11}$$

where $\hat{Z}$ is the predicted impedance from the model; F represents the new high-frequency equivalent circuit model in (8); $\hat{\theta}$ is an estimation of the true parameter vector θ and r represents constraints. Since C_1 and C_2 can be defined using (1) and (2), these two parameters are not included in θ for parameter identification.

Parameters are identified by computing the errors between measured outputs and the corresponding predicted values from models [41]. By minimizing these errors, the model is validated and parameters are identified.

$$\hat{\theta}_{opt} = arg\min_{\theta}(\varepsilon) = arg\min_{\theta}\left(\left|Z - \hat{Z}\right|\right) \tag{12}$$

where $\hat{\theta}_{opt}$ is the optimum of parameter vector θ; ε is output prediction errors and Z is the measured impedance.

In Fig.6., the parameter vector $\hat{\theta}$ is adjusted based on numerical optimization methods and iterative procedures. The parameter tuning process can be considered a nonlinear global optimization problem. This study finds that Particle Swarm Optimization (PSO) [42], [43] is well suited in this case because of its effectiveness and efficiency compared to other optimization methods. PSO is an evolutionary algorithm where a collection of candidate solutions called particles move in search space to find the best location (best objective function). The movement of particles is influenced by both their individual best location and the best location of other particles. The location and velocities of particles are updated iteratively until a stopping criterion is triggered.

Since parameters in the physics-based model possess physical significance, parameters vary within constrained bounds that are used in optimization, as shown in TABLE 2. The upper and lower bounds are set up by referencing other literature [2], [4], [10].

TABLE 2. Upper and lower bounds of parameters for optimization.

Symbol	Unit	Upper bound	Lower bound
R_1	Ω	1E4	1E2
R_{C1}	Ω	1E2	1E-10
R_{L1}	Ω	1E2	1E-10
R_2	Ω	1E4	1E2
R_{C2}	Ω	1E2	1E-10
R_{L2}	Ω	1E2	1E-10
L_1	H	1	1E-8
L_2	H	1	1E-8
L_P	H	1	1E-8

Mean Square Error (MSE) is found to be well suited as the objective function in this specific optimization case since other percentage-based error metrics, such as Mean Absolute Percentage Error (MAPE) cause misleading results [44], [45]. The objective function is defined as

$$J = \frac{1}{N}\sum_{k=1}^{N} q_k \varepsilon_k^2 \tag{13}$$

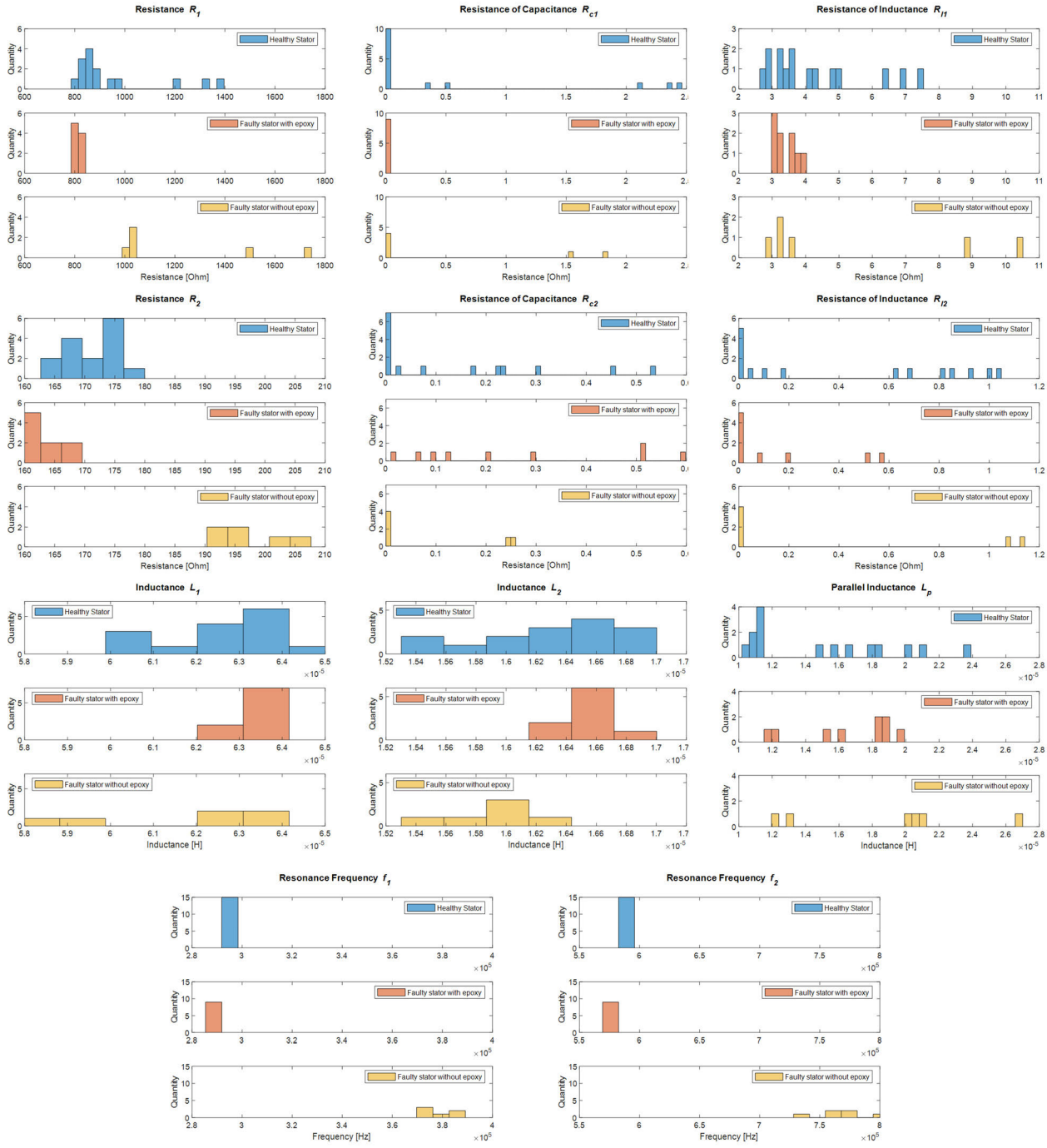

FIGURE 7. Histogram of each parameter for thirty phase windings within 10 stators.

where J is the objective function; N represents the number of data points, i.e., 171 in this case and q_k presents the kth weighting factor.

E. EXTRACTED FEATURES AND MODEL VALIDATION

Since PSO is a stochastic algorithm, 10 implementations are conducted for each phase winding to reduce randomness and find the global optimum of parameters specific for each phase winding. The histograms of each parameter for 30 phase windings within 10 stator samples are shown in Fig.7.

Despite the limited number of samples, these histograms vividly illustrate the impact of different epoxy configurations on parameters variations. For parameters R_2, f_1 and f_2, the variation ranges for stators without epoxy (stators 9 and 10) are distinct from those with epoxy (stators 1-8).

Large R_2 values of stators without epoxy have a clear physical significance as they signify dissipative phenomena originating from eddy currents in windings and laminated iron cores. For the stators without epoxy, greater magnetic flux penetrates the iron core during high-frequency excitation due to the lack of epoxy coating on top of windings. This, in turn, induces more eddy currents and results in larger dissipative phenomena.

Particularly with respect to parameters f_1 and f_2, a clear separation is evident among the three stator classes, and do not overlap. These parameters are sensitive to the epoxy-related fault conditions. The resonance frequencies that are affected by epoxy configurations of stator windings are promising indicators for fault detection.

Other parameters show less distinct variation with respect to different epoxy configurations. However, their contribution to the simulation accuracy has been validated through feature ablation studies [46], where each parameter is excluded from the model in turn to evaluate its individual impact on the overall simulation accuracy.

After identifying the optimum parameter vector $\hat{\theta}_{opt}$ for each hairpin phase winding, this parameter vector is substituted into (9) and the predicted impedance $\hat{Z}$ is simulated as illustrated in Fig. 8.

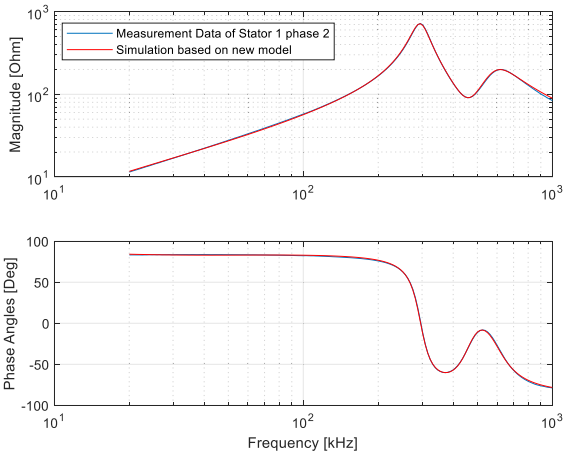

FIGURE 8. Simulation of hairpin windings based on the new model.

Fig. 8. continues to use phase winding 2 of stator 1 as an example for comparing the simulation results as in Fig.4. Fig. 8 confirms a considerable improvement for the new model compared to Fig. 4 that uses the conventional model. In Fig.8, the simulation has good agreement with measurement data across the frequency range of interest, displaying no noticeable discrepancies. The simulation based on the new model is superior to that of the conventional model, leading to reduced objective cost function values and increased simulation accuracy. For example, in Fig. 8, the objective function value decreases by 60% compared to that in Fig.4. Simulations of other phase windings based on the new model also present the same level of improvement.

The established model accurately captures a certain degree of physical configuration variation through parametric changes. However, due to measuring, modeling and parametric uncertainties introduced during the model-based feature extraction process, applying a threshold-based fault detection method becomes challenging. Therefore, a data-driven method is introduced for the classification to perform fault detection in Section. VI.

VI. DATA-DRIVEN FAULT CLASSIFICATION

After processing by the model-based method, features of hairpin windings are extracted and used as input for fault classification. The pipeline of data-driven fault classification is illustrated within the orange block in Fig. 1.

A. DATA PREPROCESSING

To integrate model-based and data-driven blocks in Fig. 1, one important step is to make sure the connecting interface is compatible with both blocks, facilitating data transfer between the successive blocks.

Features extracted from the model-based blocks are the input of the data-driven fault classification process, which includes nine optimum parameters of the equivalent circuit model and two constraints of resonant frequencies for each phase winding. With the model-based feature extraction, the original measurement data of each phase winding with the shape of (171, 4) are converted to a feature vector with a length of 11. Each feature vector represents one phase winding, and a total of 30 phase windings produce the feature data with a shape of (30,11), as presented in (14) using (10) and (11).

$$X = \begin{bmatrix} [R_1, R_{C1}, R_{L1}, R_2, R_{C2}, R_{L2}, L_1, L_2, L_P, \omega_1, \omega_2]_1 \\ \vdots \\ [R_1, R_{C1}, R_{L1}, R_2, R_{C2}, R_{L2}, L_1, L_2, L_P, \omega_1, \omega_2]_{30} \end{bmatrix} \tag{14}$$

where X is feature data extracted by the model-based block.

After this manipulation, the feature data X are ready for the following data-driven fault classification.

B. DATA VISUALIZATION

Data visualization presents patterns of data and guides preliminary algorithm selection. To visualize this high-dimensional feature data X of shape (30,11), t-distributed Stochastic Neighbor Embedding (t-SNE) [47] is applied. t-SNE maps high-dimensional data into a two-dimensional space. Similar points are concentrated whereas dissimilar points are assigned by distance points. t-SNE reveals the structure of data at a different scale. Fig. 9 shows t-SNE of feature data that include 30 phase windings.

In Fig. 9, three clusters representing different stator classes are easily observed. With the help of coloring the labels, the boundaries of the clusters are clearly defined. Stators with similar conditions are gathered, which contributes to the fault classification.

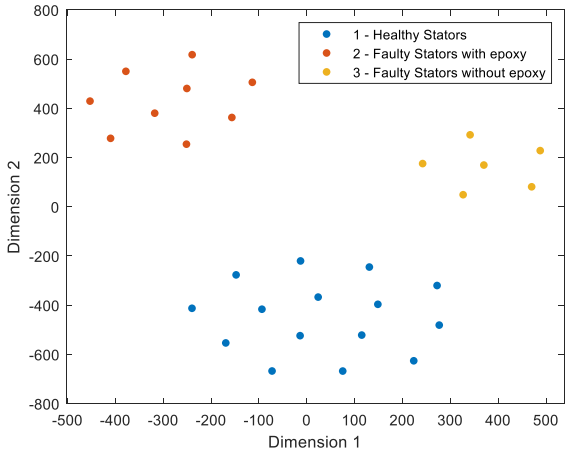

FIGURE 9. t-SNE visualization of feature data including 30 phase windings.

C. PRINCIPAL COMPONENT ANALYSIS (PCA)

As illustrated within the orange block in Fig. 1, feature data are split into both training and testing sets before inputting PCA for further feature refining. Since it is not reasonable to compare faulty stators without epoxy (stators 9 and 10) with healthy stators (stators 1 to 5) that possess different epoxy configurations side-by-side, data of stators 9 and 10 are not included in this subsection for fault detection. Data split for training and testing are detailed in TABLE 3.

TABLE 3. Training and testing samples for fault classification.

Classes	Labels	Total samples	Training	Testing
Healthy (Stators 1-5)	1	15	9	6
Faulty with epoxy (Stators 6, 7 and 8)	2	9	3	6

Using limited data for training and validation has practical implications as it is difficult to gather a large number of faulty samples in real manufacturing lines. To mirror real-world scenarios, the samples under training and testing categories of healthy and faulty classes always come from the same stator. In the healthy class, three stators are randomly selected for training and the other two stators are used for testing. In the faulty class, one stator is used for training and the remaining two stators for testing.

This study applies PCA to further refine feature data to reduce noise and uncertainties. PCA [48] is a multivariate statistical analysis method to extract features from data. It linearly extracts independent features by transforming the data in a new coordinate system with uncorrelated variables. Also, PCA reduces the dimensionality of data while preserving the maximum variation of the original data. These two properties [49] make PCA a robust tool for feature extraction within data analysis. The new extracted features are principal components, defined as:

$$T_{Training} = X_{Training} W \tag{15}$$

where $X_{Training}$ is training samples from feature data X; $T_{Training}$ is full principal components transformed from $X_{Training}$ and W is weights, whose columns are the eigenvectors of $({X_{Training}}^T X_{Training})$.

Principal components are then used as input for the following classification algorithms. They maintain the same data shape as input feature data since the full principal component transformation is employed. W remains identical while transforming testing samples, which assures the testing samples transform into the same principal component space.

D. DETECTION ALGORITHMS

Guided by insights from t-SNE data visualization, a machine learning algorithm is selected for fault classification. Since labels play a critical role in cluster separations, a supervised learning method is a priority of the algorithm selection.

This study finds Support Vector Machine (SVM) [50] is suitable for this classification case due to its effectiveness in nonlinear and multi-class classification tasks. In particular, SVM works effectively for small datasets, i.e., in the case of this study in a manufacturing environment context with limited data.

An SVM called C-Support Vector Classification [51] is applied in this study. It achieves classification by solving the following primal optimization problem:

$$\begin{aligned} \min_{w,b,\zeta} \quad & \frac{1}{2} w^T w + C \sum_{i=1}^{n} \zeta_i \\ \textit{subject to} \quad & y_i \left(w^T \phi(x_i) - b \right) \geq 1 - \zeta_i \\ & \zeta_i \geq 0, \forall i \in \{1, \ldots, n\} \end{aligned} \tag{16}$$

where w is the weight vector; b is the bias term; C is the regularization parameter; ζ is the value of the misclassification; x_i is the ith training data point; $\phi(x_i)$ maps x_i to a high-dimensional space and n is the number of data points.

SVM maps the input vector to a high-dimension feature space where a linear decision surface is constructed for binary classification. This decision surface is defined by parameters w and b, which are determined by training data. The defined decision surface is then applied to classify unseen testing data.

E. EVALUATION RESULTS

With processing by PCA and SVM, an evaluation result is illustrated in Fig. 10. Both training samples and testing samples are presented in the transformed principal component space by plotting the first two principal components. Healthy and faulty data show separate clusters where both testing healthy and testing faulty data (represented as dark blue and green dots) fall into the corresponding classes correctly.

Cross-validation is also implemented to evaluate the performance of this machine learning method. Stators 6-8 are selected for training in turns whereas the other two stators are used for testing. The healthy class keeps consistent in each cross-validation setup where three stators are

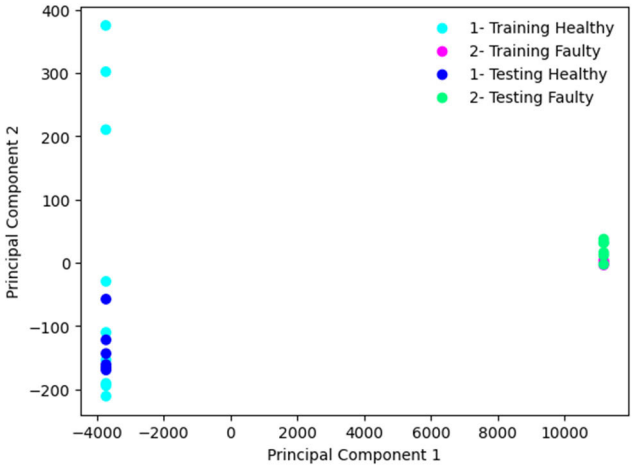

FIGURE 10. Evaluation results using SVM-based machine learning.

randomly selected for training and the other two for testing. To reduce the impact of randomness in the training process, 1000 training-evaluation cycles are conducted for each cross-validation setup and mean testing accuracy as well as overall experiment accuracy are calculated as shown in TABLE 4.

TABLE 4. Cross validation setup and evaluation results.

Cross validation No.	Training	Testing	Test Accuracy
Cross validation 1	9 Healthy+3 Faulty (Faulty: Stator 6)	6 Healthy+6 Faulty (Faulty: Stator 7 and 8)	100%
Cross validation 2	9 Healthy+3 Faulty (Faulty: Stator 7)	6 Healthy+6 Faulty (Faulty: Stator 6 and 8)	100%
Cross validation 3	9 Healthy+3 Faulty (Faulty: Stator 8)	6 Healthy+6 Faulty (Faulty: Stator 6 and 7)	100%
		Overall experiment accuracy	100%

All testing samples in both healthy and faulty classes can be successfully classified, achieving 100% overall experiment accuracy. This high accuracy benefits from some parameters, such as R_2, f_1 and f_2, extracted from the model-based method. These parameters display distinct variability in the presence of epoxy-related fault conditions, contributing to the achieved accuracy. PCA also removes noise and further refines features in data analysis despite some possible uncertainties introduced during the modeling and parameter identification process. The overall experiment accuracy improves by 5% compared to a previous work that only applied data-driven methods [31].

VII. CONCLUSION

Combining a novel physical model and a machine learning method, this paper presents a hybrid fault detection methodology that shows exceptional accuracy for epoxy fault detection of stators with hairpin windings.

In particular, a new physical model that accounts for skin and proximity effects is 60% more accurate than the conventional model when simulating high-frequency impedance behaviors. Using model parameters for fault detection, the proposed SVM-based machine learning method effectively removes noises in data, distinguishes between underlying patterns, and successfully classifies both healthy and faulty stator windings.

The hybrid method achieves higher overall accuracy than pure data-driven approaches, combining the benefits of both model-based and data-driven approaches while supplementing their deficiencies. In the meantime, it also retains model interpretability as the identified model parameters possess actual physical significance. With respect to practical implications, the proposed hybrid fault detection method focuses on manufacturing faults before stator windings enter the assembly stage, which minimizes the risk of BLDC breakdown and reduces subsequent maintenance costs. Also, such preventive maintenance enhances product delivery quality and extends the lifespan of BLDCs.

Future works will exploit the physical model of hairpin windings to generate synthetic data, simulating various operation conditions to enlarge the training dataset for a learning system. With such data augmentation, a quantitative limitation of available faulty operating data will be addressed, advancing fault detection applications and increasing accuracy.

APPENDIX
EXPERIMENTAL SETUP

Stator windings of BLDCs from a manufacturing line are used in this study. The experiment uses ten stator samples with different conditions, as shown in TABLE 5. All stators are of the same model and have a star-connected configuration.

TABLE 5. Conditions of stators, adapted from [31].

No.	Status	Epoxy	Faulty Reasons
1	Healthy	Yes	N/A
2	Healthy	Yes	N/A
3	Healthy	Yes	N/A
4	Healthy	Yes	N/A
5	Healthy	Yes	N/A
6	Faulty	Yes	Related to epoxy
7	Faulty	Yes	Related to epoxy
8	Faulty	Yes	Related to epoxy
9	Faulty	No	Related to welding
10	Faulty	No	Related to welding

Stator samples 1 to 5 with normal conditions are categorized as ‘‘healthy’’ whereas stators 6 to 10 exhibit different types of fault conditions. Specifically, stators 6-8 possess faults related to the epoxy and stators 9 and 10 carry faults related to welding, as shown in Fig. 11. (c). Since welding faults are inspected before the stators enter the epoxy coating process, stators 9 and 10 do not have an epoxy coating.

The stator samples with different epoxy coating configurations in experiments are presented in Fig. 11. (a) and (b).

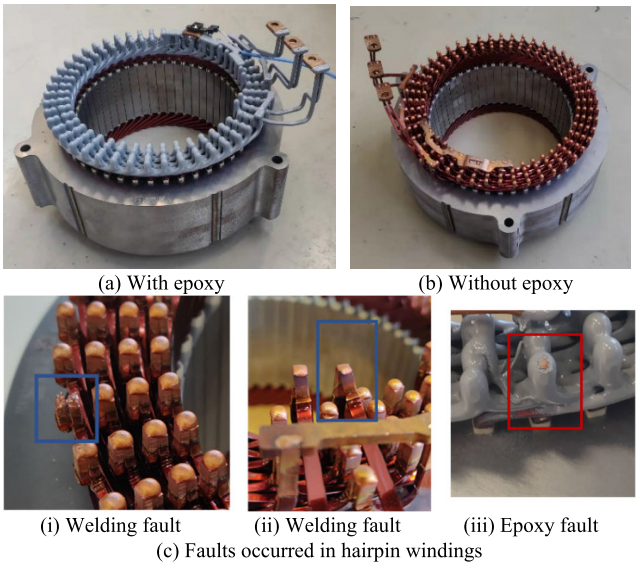

FIGURE 11. Stator samples and fault types used in experiments, adapted from [31].

The characteristics of stator windings have been found to be reflected in impedance measured at high frequencies [52], [53], [54]. In this study, the high-frequency impedance data are acquired by applying an instrument called GAMRY^{TM} [55], which measures the impedance using a sweeping sinusoidal signal from low to high frequencies. Based on experimental results reported in published literature [2], [11], the frequency range of 20 kHz to 1 MHz is selected in this study. This frequency range reportedly presented a pair of resonance frequencies with large dissipative phenomena within impedance measurement, in which healthy and faulty stator windings exhibit distinguishable patterns. Fig.12. shows the experimental setup used in this study, where one terminal of a phase winding, along with the neutral point of the stator, is connected to the GAMRY^{TM} instrument to measure the high-frequency impedance of the specific phase windings. The other two phase windings of the same stator are also measured later in turn to acquire similar data.

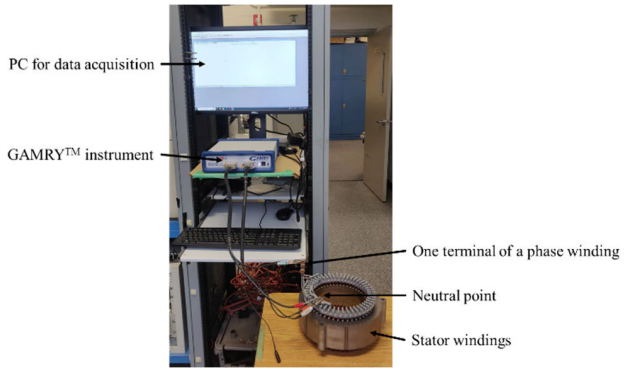

FIGURE 12. Experimental setup in the lab.

A galvanostatic test [56], which keeps the input current in constant magnitude and monitors the variation of the output voltage, is performed at each phase winding. Four pieces of information on the complex impedance are recorded: magnitude, phase angle, resistance, and reactance. The magnitude and phase angles exhibit complex impedance in the polar coordinate system whereas the resistance and reactance are in the Cartesian coordinate system.

For every high-frequency measurement, there are 171 excitation frequencies ranging from 20 kHz to 1 MHz employed. The data shape for each phase winding is (171,4), where the rows represent the excitation frequencies and the columns record the impedance information. Considering that three measurements are conducted within one stator for each phase winding, a total of 30 measurement data are available.

ACKNOWLEDGMENT

The authors want to thank Ford Motor Company for providing stator samples for experimental testing. The contributions of Ms. Zeina Tawakol in proofreading this article are gratefully acknowledged.

REFERENCES

[1] R. Krishnan, *Permanent Magnet Synchronous and Brushless DC Motor Drives*. Boca Raton, FL, USA: CRC Press, 2017.
[2] G. Grandi, D. Casadei, and U. Reggiani, "Equivalent circuit of mush wound AC windings for high frequency analysis," in *Proc. IEEE Int. Symp. Ind. Electron.*, Jun. 1997, pp. SS201–SS206.
[3] A. Boglietti, A. Cavagnino, and M. Lazzari, "Experimental high-frequency parameter identification of AC electrical motors," *IEEE Trans. Ind. Appl.*, vol. 43, no. 1, pp. 23–29, Jul. 2007.
[4] N. Idir, Y. Weens, M. Moreau, and J. J. Franchaud, "High-frequency behavior models of AC motors," *IEEE Trans. Magn.*, vol. 45, no. 1, pp. 133–138, Jan. 2009.
[5] S. Mahdavi and K. Hameyer, "High frequency equivalent circuit model of the stator winding in electrical machines," in *Proc. 20th Int. Conf. Electr. Mach.*, Sep. 2012, pp. 1706–1711.
[6] K. Tidriri, N. Chatti, S. Verron, and T. Tiplica, "Bridging data-driven and model-based approaches for process fault diagnosis and health monitoring: A review of researches and future challenges," *Annu. Rev. Control*, vol. 42, pp. 63–81, Jan. 2016.
[7] R. Isermann, "Model-based fault-detection and diagnosis-status and applications," *Annu. Rev. control*, vol. 29, no. 1, pp. 71–85, 2005.
[8] B. Mirafzal, G. L. Skibinski, R. M. Tallam, D. W. Schlegel, and R. A. Lukaszewski, "Universal induction motor model with low-to-high frequency-response characteristics," *IEEE Trans. Ind. Appl.*, vol. 43, no. 5, pp. 1233–1246, Jul. 2007.
[9] A. Consoli, G. Oriti, A. Testa, and A. L. Julian, "Induction motor modeling for common mode and differential mode emission evaluation," in *Proc. IEEE Ind. Appl. Conf. 31st IAS Annu. Meeting*, Sep. 1996, pp. 595–599.
[10] A. Boglietti and E. Carpaneto, "Induction motor high frequency model," in *Proc. Conf. Rec. IEEE Ind. Appl. Conf., 34th IAS Annu. Meeting*, Jul. 1999, pp. 1551–1558.
[11] G. Grandi, D. Casadei, and A. Massarini, "High frequency lumped parameter model for AC motor windings," in *Proc. Eur. Conf. Power Electron. Appl.*, 1997, pp. 572–578.
[12] R. M. Tallam, T. G. Habetler, and R. G. Harley, "Transient model for induction machines with stator winding turn faults," *IEEE Trans. Ind. Appl.*, vol. 38, no. 3, pp. 632–637, May 2002.
[13] Y. Wilhelm, P. Reimann, W. Gauchel, and B. Mitschang, "Overview on hybrid approaches to fault detection and diagnosis: Combining data-driven, physics-based and knowledge-based models," *Proc. CIRP*, vol. 99, pp. 278–283, Jan. 2021.

[14] W. Lang, Y. Hu, C. Gong, X. Zhang, H. Xu, and J. Deng, "Artificial intelligence-based technique for fault detection and diagnosis of EV motors: A review," *IEEE Trans. Transport. Electrific.*, vol. 8, no. 1, pp. 384–406, Mar. 2022.

[15] P. Pietrzak and M. Wolkiewicz, "Application of support vector machine to stator winding fault detection and classification of permanent magnet synchronous motor," in *Proc. IEEE 19th Int. Power Electron. Motion Control Conf. (PEMC)*, Apr. 2021, pp. 880–887.

[16] M. Singh and A. G. Shaik, "Incipient fault detection in stator windings of an induction motor using stockwell transform and SVM," *IEEE Trans. Instrum. Meas.*, vol. 69, no. 12, pp. 9496–9504, Dec. 2020.

[17] X. Dai and Z. Gao, "From model, signal to knowledge: A data-driven perspective of fault detection and diagnosis," *IEEE Trans. Ind. Informat.*, vol. 9, no. 4, pp. 2226–2238, Nov. 2013.

[18] O. Imoru, F. V. Nelwamondo, A. Jimoh, and T. R. Ayodele, "A neural network approach to detect winding faults in electrical machine," *Int. J. Emerg. Electr. Power Syst.*, vol. 22, no. 1, pp. 31–41, Feb. 2021, doi: 10.1515/ijeeps-2020-0161.

[19] A. K. Verma, S. Nagpal, A. Desai, and R. Sudha, "An efficient neural-network model for real-time fault detection in industrial machine," *Neural Comput. Appl.*, vol. 33, no. 4, pp. 1297–1310, Feb. 2021.

[20] P. Kumar and A. S. Hati, "Review on machine learning algorithm based fault detection in induction motors," *Arch. Comput. Methods Eng.*, vol. 28, no. 3, pp. 1929–1940, May 2021, doi: 10.1007/s11831-020-09446-w.

[21] X. Xu, X. Qiao, N. Zhang, J. Feng, and X. Wang, "Review of intelligent fault diagnosis for permanent magnet synchronous motors in electric vehicles," *Adv. Mech. Eng.*, vol. 12, no. 7, Jul. 2020, Art. no. 168781402094432.

[22] L. Alzubaidi, J. Zhang, A. J. Humaidi, A. Al-Dujaili, Y. Duan, O. Al-Shamma, J. Santamaría, M. A. Fadhel, M. Al-Amidie, and L. Farhan, "Review of deep learning: Concepts, CNN architectures, challenges, applications, future directions," *J. Big Data*, vol. 8, no. 1, p. 53, Mar. 2021, doi: 10.1186/s40537-021-00444-8.

[23] M. Skowron, T. Orlowska-Kowalska, and C. T. Kowalski, "Application of simplified convolutional neural networks for initial stator winding fault detection of the PMSM drive using different raw signal data," *IET Electr. Power Appl.*, vol. 15, no. 7, pp. 932–946, Jul. 2021.

[24] P. Pietrzak, M. Wolkiewicz, and T. Orlowska-Kowalska, "PMSM stator winding fault detection and classification based on bispectrum analysis and convolutional neural network," *IEEE Trans. Ind. Electron.*, vol. 70, no. 5, pp. 5192–5202, May 2023.

[25] I. Goodfellow, Y. Bengio, and A. Courville, *Deep Learning*. Cambridge, MA, USA: MIT Press, 2016.

[26] Y. LeCun, Y. Bengio, and G. Hinton, "Deep learning," *Nature*, vol. 521, no. 7553, pp. 436–444, 2015.

[27] M. Hussain, "Stator winding fault detection and classification in three-phase induction motor," *Intell. Autom. Soft Comput.*, vol. 29, no. 3, pp. 869–883, 2021.

[28] T. Zimnickas, J. Vanagas, K. Dambrauskas, A. Kalvaitis, and M. Ažubalis, "Application of advanced vibration monitoring systems and long short-term memory networks for brushless DC motor stator fault monitoring and classification," *Energies*, vol. 13, no. 4, p. 820, Feb. 2020.

[29] X.-Q. Liu, H.-Y. Zhang, J. Liu, and J. Yang, "Fault detection and diagnosis of permanent-magnet DC motor based on parameter estimation and neural network," *IEEE Trans. Ind. Electron.*, vol. 47, no. 5, pp. 1021–1030, Jul. 2000.

[30] A. Soldevila, J. Blesa, S. Tornil-Sin, E. Duviella, R. M. Fernandez-Canti, and V. Puig, "Leak localization in water distribution networks using a mixed model-based/data-driven approach," *Control Eng. Pract.*, vol. 55, pp. 162–173, Oct. 2016.

[31] Y. Zhang, Y. Huangfu, Y. Ziada, and S. Habibi, "Efficient hairpin winding fault detection using impedance measurements," *IEEE Access*, vol. 11, pp. 92838–92846, 2023.

[32] A. Agarwal and J. Lang, *Foundations of Analog and Digital Electronic Circuits*. Amsterdam, The Netherlands: Elsevier, 2005.

[33] C. K. Alexander, M. N. Sadiku, and M. Sadiku, *Fundamentals of Electric Circuits*. New York, NY, USA: McGraw-Hill, 2007.

[34] P. L. Dowell, "Effects of eddy currents in transformer windings," *Proc. Inst. Electr. Eng.*, vol. 113, no. 8, p. 1387, 1966.

[35] F. de Leon and A. Semlyen, "Time domain modeling of eddy current effects for transformer transients," *IEEE Trans. Power Del.*, vol. 8, no. 1, pp. 271–280, Aug. 1993.

[36] H. A. Wheeler, "Formulas for the skin effect," *Proc. IRE*, vol. 30, no. 9, pp. 412–424, Sep. 1942.

[37] O. Nelles, "Nonlinear dynamic system identification," in *Nonlinear System Identification*. Cham, Switzerland: Springer, 2001, pp. 547–577.

[38] P. Horowitz and W. Hill, *The Art of Electronics*. Cambridge, U.K.: Cambridge Univ. Press, 2002.

[39] Z. Popovic and B. D. Popovic, *Introductory Electromagnetics*. Upper Saddle River, NJ, USA: Prentice-Hall, 2000.

[40] L. Ljung, "System identification," in *Signal Analysis and Prediction*. Cham, Switzerland: Springer, 1998, pp. 163–173.

[41] S. Bachir, S. Tnani, J.-C. Trigeassou, and G. Champenois, "Diagnosis by parameter estimation of stator and rotor faults occurring in induction machines," *IEEE Trans. Ind. Electron.*, vol. 53, no. 3, pp. 963–973, Jun. 2006.

[42] J. Kennedy and R. Eberhart, "Particle swarm optimization," in *Proc. Int. Conf. Neural Netw.*, 1995, pp. 1942–1948.

[43] R. Poli, J. Kennedy, and T. Blackwell, "Particle swarm optimization," *Swarm Intell.*, vol. 1, no. 1, pp. 33–57, 2007.

[44] R. J. Hyndman and A. B. Koehler, "Another look at measures of forecast accuracy," *Int. J. Forecasting*, vol. 22, no. 4, pp. 679–688, Oct. 2006.

[45] S. Kim and H. Kim, "A new metric of absolute percentage error for intermittent demand forecasts," *Int. J. Forecasting*, vol. 32, no. 3, pp. 669–679, Jul. 2016.

[46] P. R. Cohen and A. E. Howe, "How evaluation guides AI research: The message still counts more than the medium," *AI Mag.*, vol. 9, no. 4, p. 35, 1988.

[47] L. Van der Maaten and G. Hinton, "Visualizing data using t-SNE," *J. Mach. Learn. Res.*, vol. 9, no. 11, pp. 2579–2605, 2008.

[48] I. T. Jolliffe, "Principal component analysis," *Technometrics*, vol. 45, no. 3, p. 276, 2003.

[49] G. Deco and D. Obradovic, *An Information-Theoretic Approach to Neural Computing*. Cham, Switzerland: Springer, 1996.

[50] C. Cortes and V. Vapnik, "Support-vector networks," *Mach. Learn.*, vol. 20, pp. 273–297, Jan. 1995.

[51] C.-C. Chang and C.-J. Lin, "LIBSVM: A library for support vector machines," *ACM Trans. Intell. Syst. Technol.*, vol. 2, no. 3, pp. 1–27, Apr. 2011.

[52] L. Lamarre and P. Picher, "Impedance characterization of hydro generator stator windings and preliminary results of FRA analysis," in *Proc. Conf. Rec. IEEE Int. Symp. Electr. Insul.*, Jun. 2008, pp. 227–230.

[53] P. A. Panagiotou, A. Lambourne, and G. W. Jewell, "Ex-situ inspection of concentrated stator coils by means of impedance spectroscopy," in *Proc. Int. Conf. Electr. Mach. (ICEM)*, Sep. 2022, pp. 2331–2337.

[54] J.-K. Park, C.-L. Jeong, S.-T. Lee, and J. Hur, "Early detection technique for stator winding inter-turn fault in BLDC motor using input impedance," *IEEE Trans. Ind. Appl.*, vol. 51, no. 1, pp. 240–247, Jan. 2015.

[55] *Basics of Electrochemical Impedance Spectroscopy*, Gamry Instrum., Complex Impedance Corrosion, Warminster, PA, USA, 2007, pp. 1–30.

[56] A. Lasia, "Electrochemical impedance spectroscopy and its applications," in *Modern Aspects of Electrochemistry*. Boston, MA, USA: Springer, 2002, pp. 143–300.

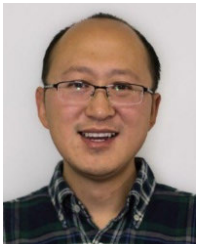

YU ZHANG received the master's degree in aerospace engineering from Carleton University, in 2019. He is currently pursuing the Ph.D. degree in mechanical engineering with McMaster University, Hamilton, ON, Canada. He has versatile working experience, including in aerospace and automotive industries. His research interests include fault detection using both model-based and data-driven methods, deep learning, and AI applications.

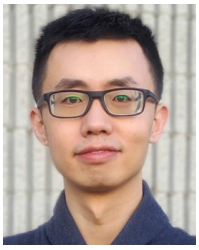

YIXIN HUANGFU (Member, IEEE) received the M.Sc. degree in mechanical engineering from Beijing Institute of Technology, in 2014, and the Ph.D. degree in mechanical engineering from McMaster University, Hamilton, ON, Canada, in 2022. From 2014 to 2017, he was a Vehicle Control Engineer with Ford Motor Research and Engineering Company Ltd., Nanjing, China. He is currently a Postdoctoral Researcher with McMaster University. His research interests include data-driven fault detection, environment perception systems for smart transportation, machine learning, and AI applications.

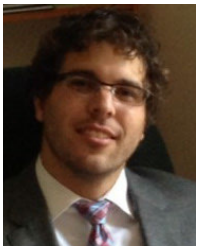

YOUSSEF ZIADA is currently the Battery Electrode Production and Cell Assembly Leader of Ford Motor Company, for the BlueOval SK joint venture. In this capacity as well as previous industry 4.0 roles, he has pursued a range of research projects in automotive manufacturing. His research interests include rapid characterization and fault detection in battery and e-motor manufacturing, predictive maintenance and physics-based AI modeling of machine tools and production equipment, and digital twins (live and static) for production systems.

SAEID HABIBI (Member, IEEE) received the Ph.D. degree in control engineering from the University of Cambridge, U.K., in 1990. He was the Chair of the Department of Mechanical Engineering, from 2008 to 2013. He is currently the Tier I Canada Research Chair and a Full Professor with the Department of Mechanical Engineering, McMaster University. He is the Founder and the Director of the Centre for Mechatronics and Hybrid Technologies (CMHT). CHMT has created one of the most advanced and best equipped automotive research laboratories in Canada and internationally specializing in predictive algorithms, tracking, prognostics, and diagnostics. CMHT currently supports a number of large projects and being a resource to automotive companies and start-ups. CMHT research is supported by industry and funding from Ontario Research Fund Research Excellence Awards and NSERC. He has published over 200 peer-reviewed articles. His academic background includes research into artificial intelligence, intelligent control, state and parameter estimation, fault diagnosis, and prediction. He is a fellow of American Society of Mechanical Engineers (ASME) and Canadian Society of Mechanical Engineers (CSME).